Hsc70 chaperone activity is required for the cytosolic slow axonal transport of synapsin

Archan Ganguly,[1] Xuemei Han,[2]* Utpal Das,[1]* Lina Wang,[5] Jonathan Loi,[5] Jichao Sun,[5] Daniel Gitler,[3] Ghislaine Caillol,[4] Christophe Leterrier,[4] John R. Yates III,[2] and Subhojit Roy[5,6]

[1]Department of Pathology, University of California, San Diego, La Jolla, CA
[2]Department of Cell Biology, The Scripps Research Institute, La Jolla, CA
[3]Department of Physiology and Cell Biology, Faculty of Health Sciences, Ben-Gurion University of the Negev and Zlotowski Center for Neuroscience, Beer-Sheva, Israel
[4]Aix Marseille Université, Centre National de la Recherche Scientifique, NICN UMR7259, Marseille, France
[5]Department of Pathology and Laboratory Medicine and [6]Department of Neuroscience, University of Wisconsin-Madison, Madison, WI

Soluble cytosolic proteins vital to axonal and presynaptic function are synthesized in the neuronal soma and conveyed via slow axonal transport. Our previous studies suggest that the overall slow transport of synapsin is mediated by dynamic assembly/disassembly of cargo complexes followed by short-range vectorial transit (the "dynamic recruitment" model). However, neither the composition of these complexes nor the mechanistic basis for the dynamic behavior is understood. In this study, we first examined putative cargo complexes associated with synapsin using coimmunoprecipitation and multidimensional protein identification technology mass spectrometry (MS). MS data indicate that synapsin is part of a multiprotein complex enriched in chaperones/cochaperones including Hsc70. Axonal synapsin–Hsc70 coclusters are also visualized by two-color superresolution microscopy. Inhibition of Hsc70 ATPase activity blocked the slow transport of synapsin, disrupted axonal synapsin organization, and attenuated Hsc70–synapsin associations, advocating a model where Hsc70 activity dynamically clusters cytosolic proteins into cargo complexes, allowing transport. Collectively, our study offers insight into the molecular organization of cytosolic transport complexes and identifies a novel regulator of slow transport.

Introduction

The vast majority of axonal and presynaptic proteins are synthesized in the neuronal soma and conveyed via axonal transport. Pulse-chase radiolabeling studies in a variety of organisms—mice, rats, guinea pigs, rabbits, *Aplysia californica*, *Xenopus laevis*, and others—have found that newly synthesized proteins are conveyed into axons in two distinct overall rates called fast and slow axonal transport (Black and Lasek, 1979; Brady et al., 1981; Garner and Lasek, 1981, 1982; Koike and Matsumoto, 1985; Baitinger and Willard, 1987; Sekimoto et al., 1991; Dillman et al., 1996; Mills et al., 1996; Yuan et al., 1999). Whereas the fast component carries membranous/membrane-anchoring proteins at rates of ∼100–400 mm/d, the slow component is composed of cytosolic and cytoskeletal cargoes moving at mean rates that are orders of magnitude slower (∼0.2–10 mm/d; Grafstein and Forman, 1980; Roy, 2014; Black, 2016). Slow transport can be further resolved into a relatively faster cohort containing cytosolic proteins, moving at mean rates of ∼2–10 mm/d (known as slow component b [SCb]), and a slower group carrying mainly cytoskeletal proteins at mean rates of ∼0.2–3 mm/d (called slow component a or SCa; Black and Lasek, 1980; Garner and Lasek, 1982; Lasek et al., 1984).

Though the radiolabeling experiments defined overall rate classes, the transported cargoes could not be visualized by these techniques. More recently, we developed live assays to visualize slow cytosolic transport in cultured neurons. In brief, when a discrete pool of cytosolic molecules is photoactivated in the axon shaft, the dispersion of fluorescent molecules has a slow anterograde bias, that likely represents slow transport (Scott et al., 2011; Tang et al., 2012, 2013). Particle tracking suggests that this overall biased transit is mediated by the assembly/disassembly of cargoes and short spurts of vectorial movement, advocating a model wherein cytosolic molecules dynamically assemble into cargo complexes that are subsequently transported (the "dynamic recruitment" model; Roy, 2014). Though these particle kinetics have been documented by several studies (Scott et al., 2011; Tang et al., 2012, 2013; Twelvetrees et al., 2016), the underlying basis for this behavior is unknown. We reasoned that understanding the composition of transport complexes might offer clues, which was the motivation for this work.

---

*X. Han and U. Das contributed equally to this paper.

Correspondence to Subhojit Roy: roy27@wisc.edu

Abbreviations used: coIP, coimmunoprecipitation; DIV, days in vitro; FFT, Fast Fourier transform; Hsp, heat shock protein; IP, immunoprecipitation; MS, mass spectrometry; MudPIT, multidimensional protein identification technology; PAGFP, photoactivatable GFP; TKO, triple knockout.

Although the idea that cytosolic cargoes moving in slow transport may be organized as multiprotein complexes has been around for decades, evidence for this notion is limited, largely resting on biochemical fractionation experiments where SCb proteins settle in high-density fractions, behaving like protein complexes (Lorenz and Willard, 1978; Tytell et al., 1981; Garner and Lasek, 1982; Scott et al., 2011). Though a handful of cytosolic proteins have been shown to associate in coimmunoprecipitation (coIP) experiments (Black et al., 1991), even an inventory of any SCb complex is lacking. Using multidimensional protein identification technology (MudPIT) mass spectrometry (MS; MudPIT-MS; McDonald et al., 2004), in this study we characterize a multiprotein complex containing the archetypal SCb protein synapsin-I (hereafter called synapsin; Baitinger and Willard, 1987; Paggi and Petrucci, 1992) from mouse brain fractions. Brains from mice lacking all synapsins were used as controls, providing confidence in the datasets. Native cytosolic protein assemblies in axons were also visualized by two-color superresolution imaging, offering the first nanometer-level view of SCb complexes. Our study reveals a higher-order organization of synapsin with several classes of cytosolic proteins and implicates heat shock proteins (Hsps) as potential regulators of slow axonal transport.

Results

Isolation of synapsin complexes from brain and proteomic strategies

Our overall goal was to isolate synapsin complexes from brain fractions expected to be enriched in SCb proteins and then identify peptide constituents by MudPIT-MS. In previous studies, we examined cytosolic proteins, including synapsin, in mouse brain fractions from synaptosomal (P2) and nonsynaptosomal (or "synaptosome-depleted" S100 and P100) fractions, reasoning that the latter would contain the synapsin pool conveyed in SCb (Fig. 1 A; Scott et al., 2011; Tang et al., 2013). To get an inventory of the synapsin-associated proteins, in this study, we immunoprecipitated synapsin from each of these fractions (P2, S100, and P100) using protocols described by Scott et al. (2011). In brief, immunoprecipitation (IP) was performed under nondenaturing conditions in the presence of low–ionic strength buffers (to help preserve native interactions). Thereafter, the protein composition in the resultant samples was determined using MudPIT-MS (Fig. 1 B). As controls, we used mouse brains lacking all three known synapsin isoforms (synapsin-I/-II/-III), hereafter called synapsin triple knockout (TKO) mice (Gitler et al., 2004a). Specifically, we performed identical synapsin coIP experiments with TKO mouse brain lysates and identified peptide constituents by MudPIT-MS to generate control peptide lists, reasoning that the peptides immunoprecipitated in this case should be a result of nonspecific associations.

Silver-stained gels of IP fractions suggest that synapsin was associated with other proteins (Fig. 1 C). For MS analyses, in brief, the immunoprecipitated samples from WT and TKO brains were reduced, alkylated, protease digested, and separated by liquid chromatography before MS analysis. Tandem mass spectra were generated and matched to peptides in a mouse database. As shown in the raw MS spectrum counts (Fig. 1 D), synapsins could be readily immunoprecipitated from WT brains but were virtually absent in TKO samples. Spectrum counts for each protein from several independent runs were normalized

and averaged to obtain final spectrum counts for a given protein in both WT and TKO samples (Fig. 2, see the Protein identification through MudPIT-MS analysis section of Materials and methods for further details). Thereafter, we applied the following inclusion criteria to identify proteins associated with synapsin in the various brain fractions. First, we included proteins that were detected in WT but not in TKO samples, reasoning that these peptides were likely candidates for synapsin-associated proteins (Fig. 2). Additionally, we also included peptides with WT spectrum counts that were two or more times that of TKO. Using these two criteria, the final lists had ∼2,000–3,000 proteins in each fraction, and these were considered to be putative synapsin-interacting proteins (for complete lists, see Tables S1, S2, and S3).
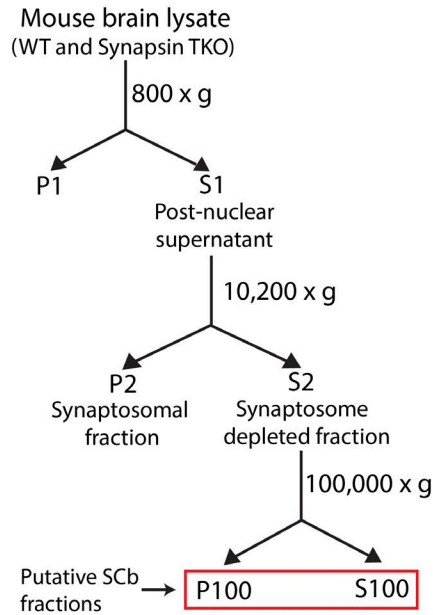
Characterization of synaptosomal and nonsynaptosomal fractions

Next, we examined synapsin-associated proteins in the synaptosomal (P2) fractions. The synaptic proteome was enriched in metabolic enzymes and cytoskeletal (and not membrane-spanning) proteins, consistent with the known biology of the cytosolic protein synapsin (Fig. 3 A). Although synapsin is an established synaptic protein and has been studied in detail (Cesca et al., 2010; Giovedí et al., 2014), we are not aware of any comprehensive and unbiased proteomic studies on synapsin-interacting proteins at synapses. Nevertheless, candidate-based studies have identified some, and we asked whether these proteins were also detected in our MS experiments. Indeed, several reported synapsin interactors (CamKII, calmodulin, endophilin, actin, etc.) were also present in our synaptosomal/P2 list (Fig. 3 B), whereas some others were detected in nonsynaptosomal fractions (for full lists, see Table S4). Most of the proteins detected in this study have also been reported in previous MS studies of synaptosomes (Peng et al., 2004; Collins et al., 2005; Takamori et al., 2006). Collectively, these data provide further confidence in the validity of our IP protocols and proteomics approach.
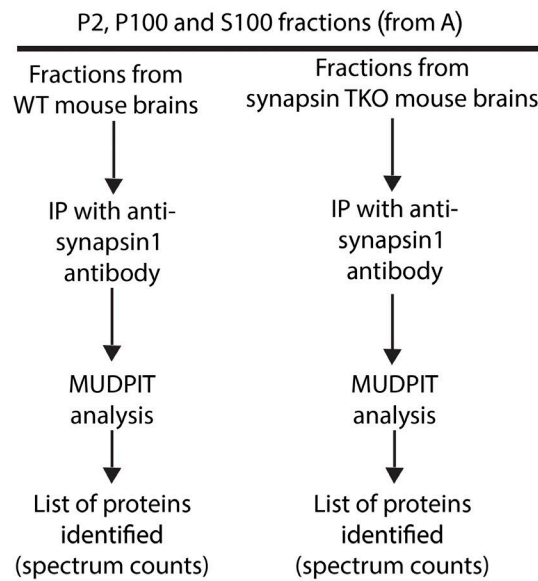
Examination of the P100/S100 (nonsynaptosomal) fractions—expected to contain SCb proteins—revealed that these two cohorts were comprised of proteins belonging to related functional groups (Fig. 4 A), though the exact peptides varied (Tables S2 and S3). Interestingly, among the proteins pulled down with synapsin was a large group of chaperone and cochaperone proteins with relatively high spectral counts and functional interconnectivity, including the major constitutive cellular chaperone Hsc70 (Fig. 4, B and C). As Hsc70 has well-known functions in organizing protein complexes in many cellular contexts (Bukau and Horwich, 1998) and have also been posited to play a role in organizing SCb complexes (de Waegh and Brady, 1989; Black et al., 1991), we wondered whether they might also play a role in clustering synapsin molecules and regulating their transport. Like other cytosolic proteins, Hsc70 and other Hsps are also conveyed in SCb and are well situated to play a regulatory role (Clark and Brown, 1985; de Waegh and Brady, 1989; Black et al., 1991; Sekimoto et al., 1991; Bourke et al., 2002).

As synapsin–Hsc70 associations have not been described previously, we first characterized their association using HEK293 cells. Specifically, we transfected HEK293 cells, which have high levels of endogenous Hsc70, with either the full-length GFP-tagged synapsin or various GFP-tagged deletion mutants. Previous studies have examined the roles of various synapsin domains in some detail (Fig. 4 D, top),
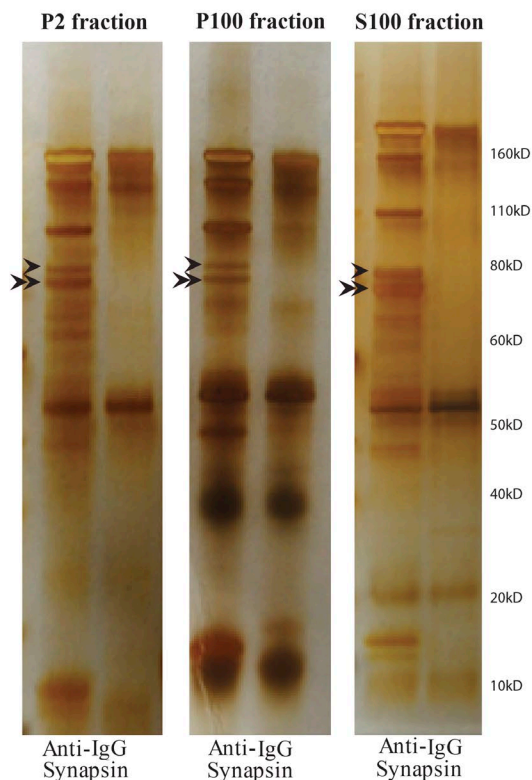
A Fractionation strategy

Mouse brain lysate
(WT and Synapsin TKO)

800 x g

P1   S1
Post-nuclear
supernatant

10,200 x g

P2   S2
Synaptosomal   Synaptosome
fraction   depleted fraction

100,000 x g

Putative SCb → P100   S100
fractions

B Overall strategy for co-IP/MudPIT-MS analysis

P2, P100 and S100 fractions (from A)

Fractions from   Fractions from
WT mouse brains   synapsin TKO mouse brains

IP with anti-   IP with anti-
synapsin1   synapsin1
antibody   antibody

MUDPIT   MUDPIT
analysis   analysis

List of proteins   List of proteins
identified   identified
(spectrum counts)   (spectrum counts)

C Silver stained gels of IP fractions

P2 fraction   P100 fraction   S100 fraction

160kD
110kD
80kD
60kD
50kD
40kD
20kD
10kD

Anti-IgG   Anti-IgG   Anti-IgG
Synapsin   Synapsin   Synapsin

D Synapsin spectral counts in IP fractions

Synapsin I

Raw Spectrum Counts

8000
6000
4000
2000
0

WT TKO   WT TKO   WT TKO   WT TKO
   S2   P2   S100   P100

Synapsin II

Raw Spectrum Counts

4000
3000
2000
1000
0

WT TKO   WT TKO   WT TKO   WT TKO
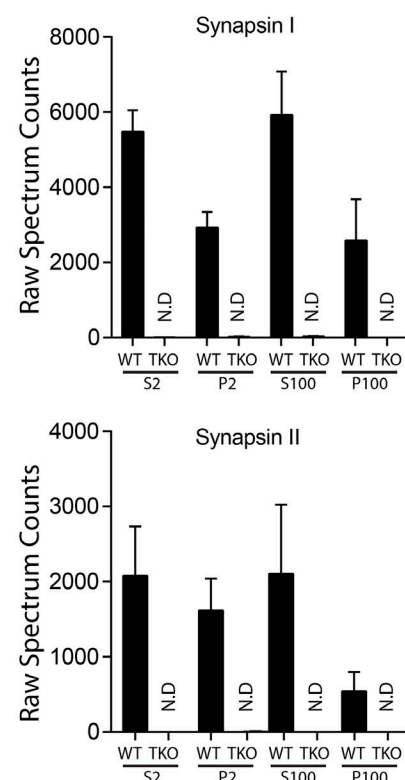   S2   P2   S100   P100

Figure 1. **Isolation of synapsin-associated protein complexes from mouse brains.** (A) Whole-brain lysates from WT or synapsin TKO mice were differentially fractionated to obtain synaptosomal (P2) and synaptosome-depleted fractions (S2). The latter were further subfractionated into P100 and S100 fractions by high-speed centrifugation (red box, putative SCb fractions; see the Isolation of synapsin complexes… section of Results). (B) Synaptosomal (P2) and nonsynaptosomal fractions (P100 and S100) from A were coimmunoprecipitated with an anti-synapsin antibody under nondenaturing conditions. CoIP fractions were subjected to MudPIT-MS to identify peptides. TKO brain lysates were used as negative controls. (C) Silver-stained gels of synapsin coIP fractions from WT brain lysates (P2, P100, and S100) suggest the presence of polypeptides associated with synapsin. Single arrowheads represent synapsin-Ia, double arrowheads represent synapsin-Ib (note IgG controls, right lanes). (D) Raw spectrum counts of synapsins-I and -II from various coIP fractions as detected by MudPIT-MS. Note spectrum counts are high in WT fractions but undetectable in TKO lysates.
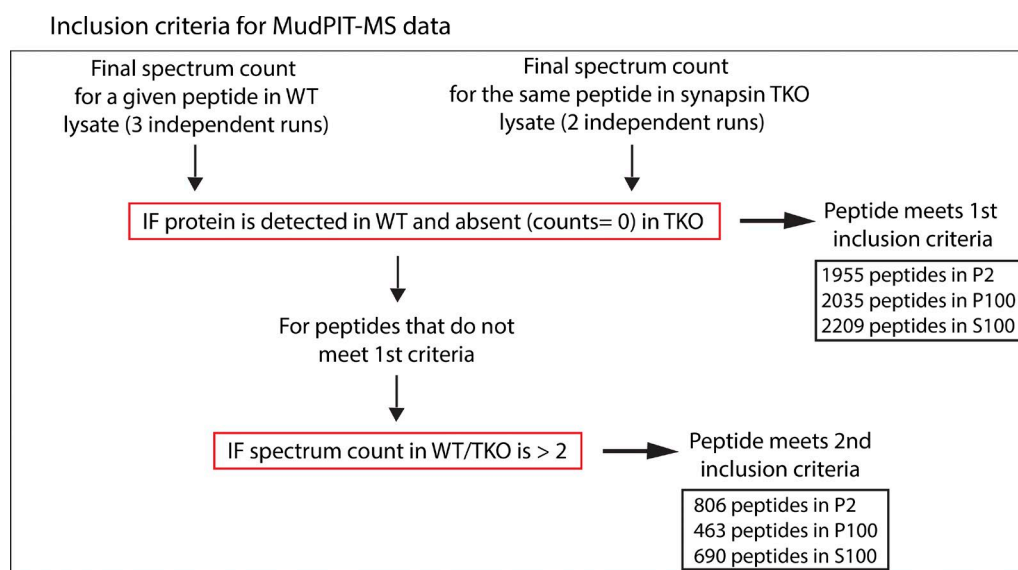
Inclusion criteria for MudPIT-MS data

Figure 2. **Criteria for including synapsin-interacting peptides identified by MudPIT-MS analysis.** Raw spectrum counts for a given protein from WT and TKO lysates were normalized and averaged to obtain final spectral counts using conventional strategies as detailed in the Isolation of synapsin complexes… section of Results. The following inclusion criteria were then applied to determine synapsin-associated proteins. First, peptides detected in WT but not in the TKO lysates (spectrum count = 0) were included. Second, peptides with final spectrum counts of twofold or more than TKO fractions were also included in the list. The final numbers of proteins are indicated in the black boxes. IF, immunofluorescence.

and we exploited this information to examine Hsc70–synapsin interactions (Gitler et al., 2004b; Cesca et al., 2010). Synapsin was immunoprecipitated from these samples using an anti-GFP antibody (Fig. 4D). Although no Hsc70 was coimmunoprecipitated in cells transfected with GFP alone, robust levels of Hsc70 were coimmunoprecipitated from cells containing GFP:synapsin constructs (Fig. 4 D, left two lanes). Our data further suggest that the D-domain of synapsin associates with Hsc70 (Fig. 4 D, right four lanes).

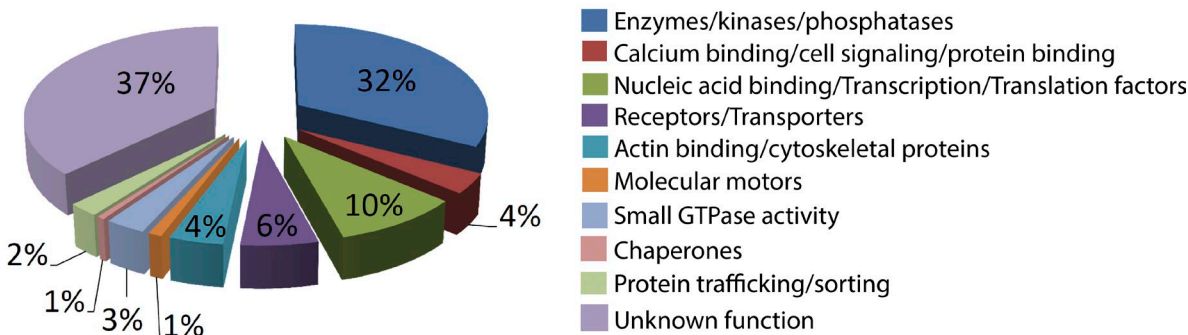### Visualization of synapsin–Hsc70 complexes by two-color superresolution microscopy

The preceding experiments suggest that synapsin and Hsc70 are members of a supramolecular complex. To further define this complex and explore underlying mechanisms, we turned to cultured hippocampal neurons, a model system that allows high-resolution studies and live-imaging experiments. Endogenous synapsin and Hsc70 were distributed as punctate structures in soma, dendrites, and axons in cultured neurons, along with a low-level diffuse distribution, as seen by routine light microscopy (Fig. S1 A). Interestingly, we noticed that synapsin and Hsc70 particles were often in close approximation in axons, in addition to some overlap (see representative images and quantification in Fig. S1, A–C). This apposition suggests that the two proteins synapsin and Hsc70 might be part of larger complexes containing other proteins that remain unlabeled in these experiments.

To examine this in more detail, we used two-color superresolution microscopy to visualize endogenous synapsin and Hsc70 in axons at nanometer resolution using DNA-PAINT, a variation of point accumulation for imaging in nanoscale topography (see the Superresolution imaging of endogenous synapsin… section of Materials and methods; Fig. 5 A; Jungmann et al., 2014). Representative data from these superresolution experiments are shown in Fig. 5 C (for a corresponding widefield image, see Fig. 5 B). Interestingly, at this resolution (25 nm in

the x/y plane), we noticed coclusters of synapsin and Hsc70 molecules distributed along the axon shaft (Fig. 5, C' and C''), suggesting that these two proteins are not randomly distributed but instead are organized in some manner. Also note that the overall spatial organization of synapsin–Hsc70 clusters at this resolution, with "gaps" within a seemingly clustered complex (see dotted circles in Fig. 5 C'', for instance), suggest the presence of other unstained proteins within these complexes, pointing to a scenario in which synapsin and Hsc70 are part of a larger transport complex (though some of this might also be space occupied by the antibodies themselves).

We also wrote algorithms to quantitatively analyze the size of synapsin–Hsc70 puncta and their proximity to each other in the superresolution dataset. Details are provided in the Superresolution imaging of endogenous synapsin… section of Materials and methods and are summarized here. To obtain particle size, bounded rectangles were drawn around the irregularly shaped puncta, and particle diameter was estimated as shown in Fig. 5 D (schematic and histogram; mean diameters of Hsc70 and synapsin particles were 39.8 and 37.4 nm, respectively). To ascertain proximity of the synapsin–Hsc70 puncta, we first calculated the intensity-weighted center of mass of each punctum and then asked whether the centers of neighboring synapsin and Hsc70 puncta were within a user-defined distance to each other. In principle, the user-defined distance should minimally reflect the actual sizes of synapsin–SCb complexes; however, as this is unknown, we reasoned that a conservative estimate would be the sum of the mean diameters of synapsin and Hsc70 puncta, which is ∼77 nm (39.8 nm + 37.4 nm). As shown in Fig. 5 E (graph), using these criteria, ∼40–60% Hsc70 particles were in close approximation to synapsin (numbers of synapsin particles in close approximation to Hsc70 were also similar; not depicted; also note that the percentages might be an underestimation as the total SCb complex may be larger). These data suggest that native synapsin–Hsc70 complexes in axons are heterogeneous and also offer the first glimpse into the overall size of SCb complexes.

A Composition of synaptosomal (P2) fraction

Legend:
- Enzymes/kinases/phosphatases
- Calcium binding/cell signaling/protein binding
- Nucleic acid binding/Transcription/Translation factors
- Receptors/Transporters
- Actin binding/cytoskeletal proteins
- Molecular motors
- Small GTPase activity
- Chaperones
- Protein trafficking/sorting
- Unknown function

37% 32% 10% 4% 6% 4% 2% 1% 3% 1%

B Reported synapsin interactors that were identified in P2 fractions

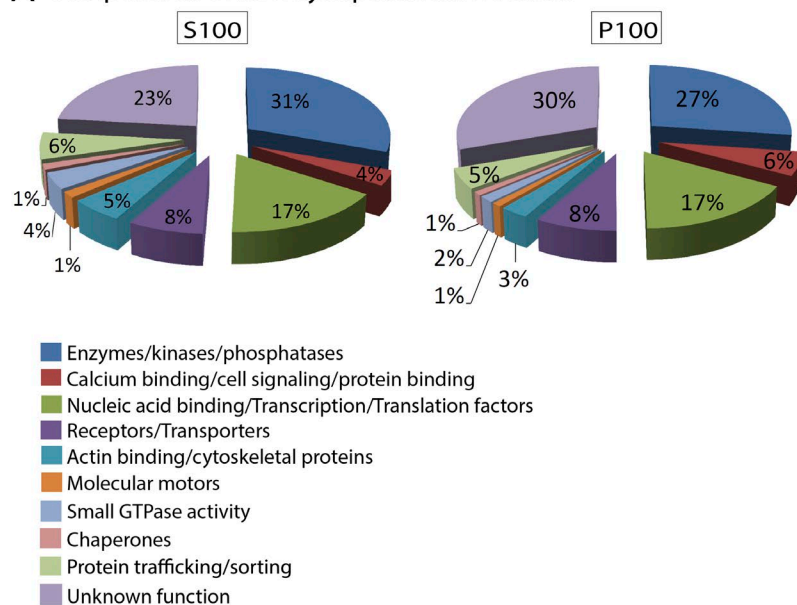| Reported Synapsin interactors	Reference
Actin	Bähler et al., J Cell Biol. 1989
α-synuclein	Woods et al., J Biol Chem. 2007
Armadillo repeat containing	Huttlin et al., Cell. 2015
Bridging integrator	Onofri et al., J Biol Chem. 2000
Calmodulin	Heierhorst et al., Biochem J. 1999
CaMKII	Benfenati et al., Nature. 1992
DEAD box helicase	Havugimana et al., Cell. 2012
Endophilin A1	Modregger et al., J Biol Chem. 2003
Endophilin A3	Modregger et al., J Biol Chem. 2003
GTF3C2/TFIIIC-β/TFIIIC110	Hein et al., Cell. 2015
PI3K	Onofri et al., J Biol Chem. 2000
PSMD2/TRAP2 (proteasome 26S subunit)	Hein et al., Cell. 2015
RB1CC1/ATG17/CC1/FIP200/PPP1R131	Arroyo et al., J Mol Biol. 2015
Synapsin II	Hosaka M, J Biol Chem. 1999
Tubulin	Aubert-Foucher E, Font B. Biochemistry. 1990
Vimentin	Stelzl et al., Cell. 2005

Figure 3. **Characterization of the synapsin proteome from the synaptosomal fraction.** (A) Peptides meeting inclusion criteria from the synaptosomal fraction (P2) were classified based on the molecular function. Note that metabolic enzymes, transcription factors, and cytoskeletal elements constitute a large fraction of the identified peptides as expected ("%" represents the number of proteins in the functional group per total number proteins in the fraction × 100). (B) Table of known synapsin interactors detected in the synaptosomal fraction (also see Table S4).

Hsc70 inactivation attenuates the slow axonal transport of synapsin
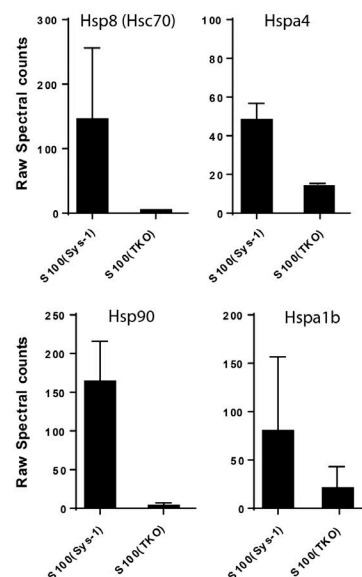
Though these data suggest that synapsin and Hsc70 are members of a higher-order assembly, the specific role of Hsc70 in this complex, if any, is unclear. Hsc70 is a constitutive member of the Hsp family with intrinsic ATPase activity that can hydrolyze ATP to ADP. The ADP-bound form has a higher affinity for its binding partners, and inactivation of the ATPase activity is expected to interrupt peptide binding as well (Huang et al., 1993; Bukau et al., 2006; DeGeer et al., 2015). Because Hsc70 has established functions in protein folding and maintenance of physiological macromolecular assemblies, we asked whether this chaperone may also play a role in clustering synapsin complexes and facilitating slow transport.

To test this idea, we attenuated the ATPase activity of Hsc70 in cultured neurons both pharmacologically and genetically and visualized slow axonal transport of synapsin. To inactivate Hsc70, we used a well-characterized small molecule inhibitor (VER155008) that blocks Hsc70 ATPase activity by associating with its ATP-binding domain (Massey et al., 2010). As a complementary genetic approach, we used a dominant-negative Hsc70 mutant (D10N) that impairs ATP hydrolysis (Huang et al., 1993; DeGeer et al., 2015). To visualize slow transport of synapsin, we used a photoactivation assay previously established in our laboratory (Roy et al., 2011; Scott et al., 2011; Tang et al., 2013). In this assay, neurons were transfected with photoactivatable GFP (PAGFP)-tagged synapsin, a discrete region of interest (ROI) within the axon was photoacti-
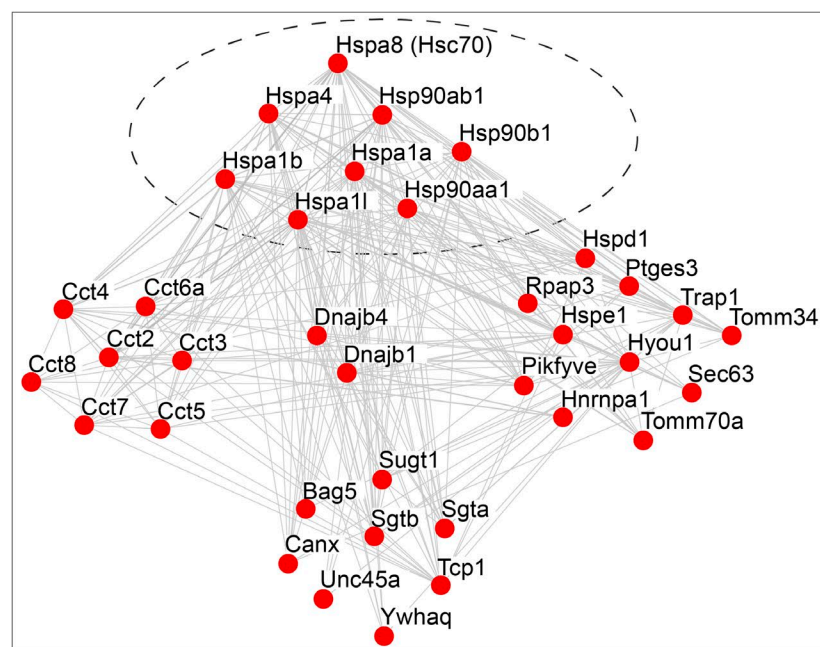
A Composition of non-synaptosomal fractions

S100

P100

- ■ Enzymes/kinases/phosphatases
- ■ Calcium binding/cell signaling/protein binding
- ■ Nucleic acid binding/Transcription/Translation factors
- ■ Receptors/Transporters
- ■ Actin binding/cytoskeletal proteins
- ■ Molecular motors
- ■ Small GTPase activity
- ■ Chaperones
- ■ Protein trafficking/sorting
- ■ Unknown function

B Raw spectral counts of Hsps (S100)

C Protein interactome of non-synaptosomal chaperones (S100)

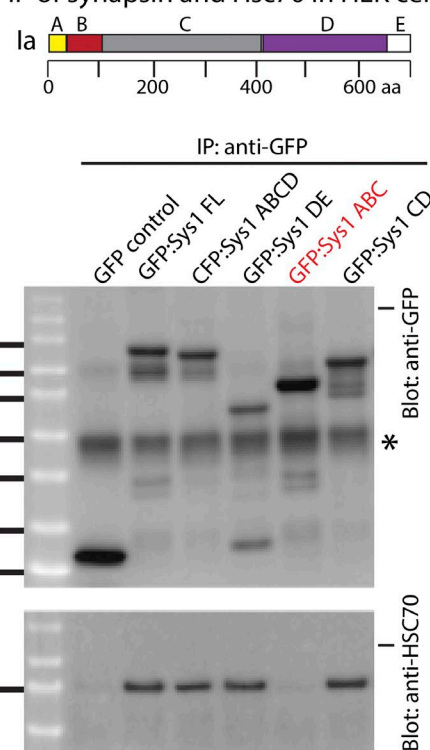**D** Co-IP of synapsin and Hsc70 in HEK cells

Figure 4. **Characterization of synapsin protein complexes from nonsynaptosomal fractions.** (A) Functional categorization of peptides identified in the nonsynaptosomal (P100 and S100) fractions ("%" represents number of proteins in the functional group per total number proteins in the fraction × 100). (B) Bar graphs showing raw spectrum counts for selected chaperones detected in the S100 fraction. Error bars show means ± SEM. (C) Protein–protein interaction map of the chaperones identified in the S100 fraction. Individual proteins are highlighted by red dots, and protein–protein interactions are indicated by light gray lines. The dashed circle highlights the Hsp peptides. (D) CoIP of synapsin and Hsc70 in HEK293T cells. HEK cells were either transfected with the full-length GFP-tagged synapsin or various GFP-tagged deletion mutants containing only some of the domains that make up the protein (a schematic of various synapsin domains is on top). The transfected synapsin and endogenous Hsc70 was detected by anti-GFP and anti-Hsc70 antibodies, respectively. Note that only the synapsin deletion lacking the D-domain failed to associate with Hsc70 (fifth lane from left, bottom gel). The asterisk indicates IgG heavy chain. Molecular mass is indicated in kilodaltons.
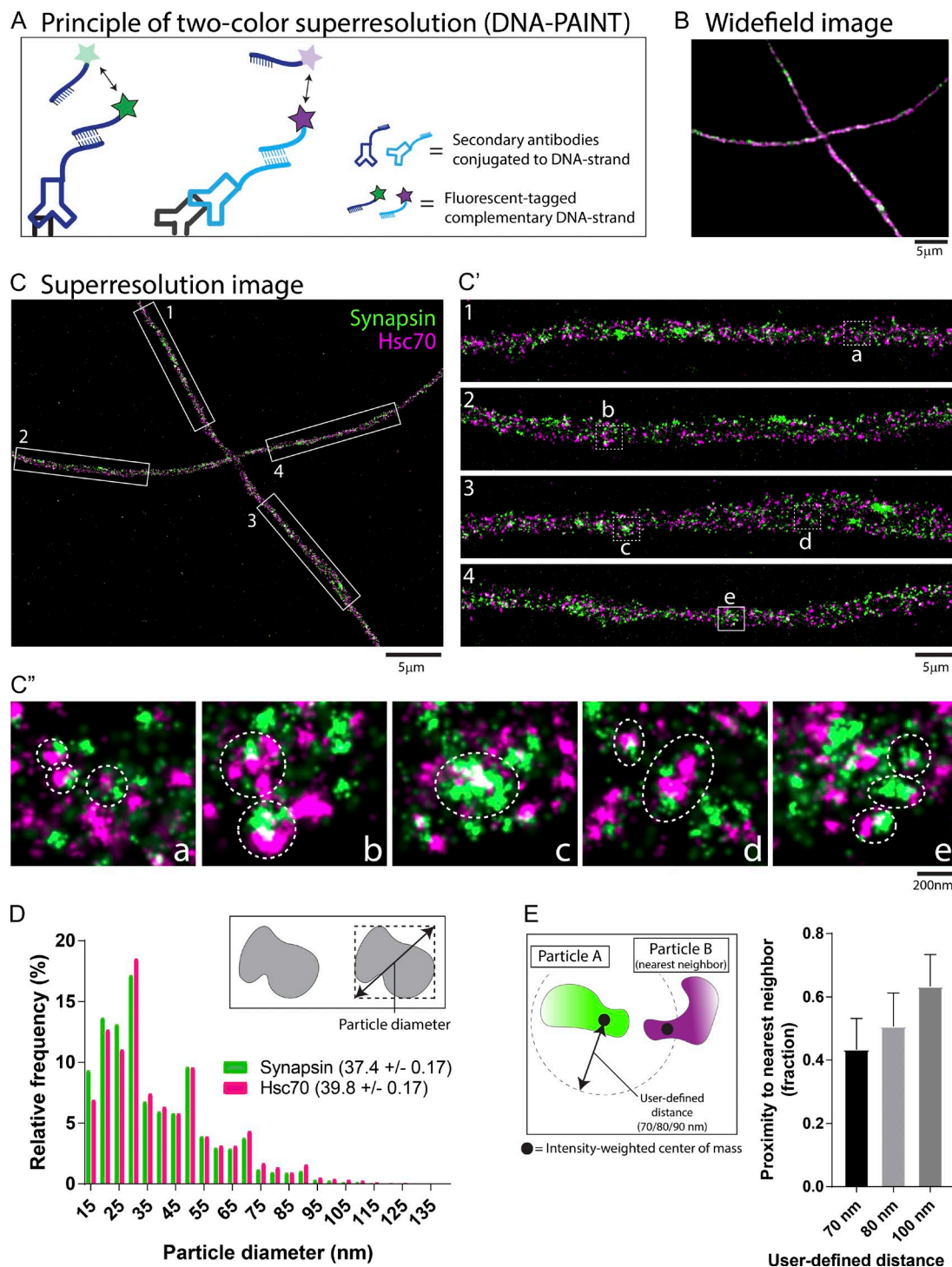
A Principle of two-color superresolution (DNA-PAINT)

= Secondary antibodies conjugated to DNA-strand

= Fluorescent-tagged complementary DNA-strand

B Widefield image

5μm

C Superresolution image

Synapsin
Hsc70

5μm

C'

5μm

C"

200nm

D

Relative frequency (%)

Particle diameter

Synapsin (37.4 +/- 0.17)
Hsc70 (39.8 +/- 0.17)

Particle diameter (nm)

E

Particle A   Particle B (nearest neighbor)

User-defined distance (70/80/90 nm)

● = Intensity-weighted center of mass

Proximity to nearest neighbor (fraction)

70 nm   80 nm   100 nm

User-defined distance

Figure 5. **Coclustering of endogenous synapsin and Hsc70 in axons visualized by two-color superresolution microscopy.** (A) Principle of DNA-PAINT. Note weak hybridization between DNA strands leads to fluorophore "blinking," allowing superresolution imaging. (B and C) Widefield and corresponding two-color superresolution image of axonal synapsin and Hsc70. Progressively zoomed insets from C are shown in C' and C". Note coclusters of synapsin and Hsc70 (some highlighted with dashed circles in C"). (D and E) Quantifications of axonal superresolution data. (D) Size of particles was ~40 nm; and (E) ~60% of the synapsin particles were within 100 nm of Hsc70 particles, suggesting coclustering.

vated, and the photoactivated population was tracked over time by live imaging (Fig. 6 A, schematic).

Under physiological conditions, the dispersion of photoactivated synapsin molecules is anterogradely biased (Fig. 6 B, top; Scott et al., 2011; Tang et al., 2013). However, attenuation of Hsc70 ATPase activity blocked this anterograde bias,

actually introducing a retrograde bias. Quantitative data from these experiments are shown in Fig. 6 C. Note that the y axis (intensity center shift) in these graphs represents displacement of the centroid of the photoactivated pool over time (positive numbers indicate anterograde transport; for details see the Microscopy, live imaging/analysis, and synaptic targeting section
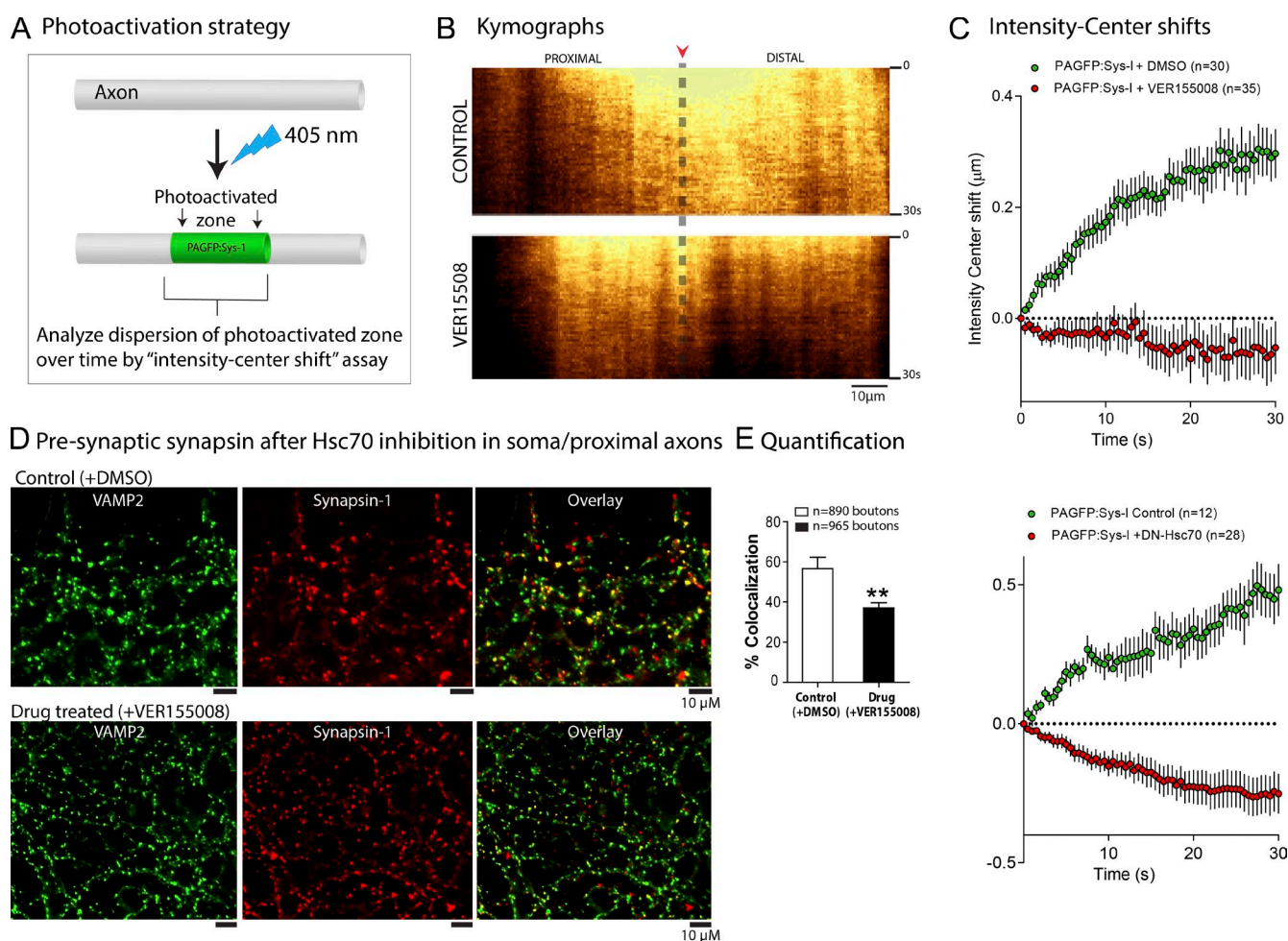
A Photoactivation strategy

Axon

405 nm

Photoactivated zone

PAGFP:Sys-1

Analyze dispersion of photoactivated zone over time by "intensity-center shift" assay

B Kymographs

PROXIMAL   DISTAL

CONTROL

VER15508

10µm

C Intensity-Center shifts

○ PAGFP:Sys-I + DMSO (n=30)
● PAGFP:Sys-I + VER155008 (n=35)

○ PAGFP:Sys-I Control (n=12)
● PAGFP:Sys-I +DN-Hsc70 (n=28)

D Pre-synaptic synapsin after Hsc70 inhibition in soma/proximal axons

Control (+DMSO)

VAMP2 | Synapsin-1 | Overlay

10 µM

Drug treated (+VER155008)

VAMP2 | Synapsin-1 | Overlay

10 µM

E Quantification

□ n=890 boutons
■ n=965 boutons

**

Control (+DMSO) | Drug (+VER155008)

Figure 6. **Inactivation of Hsc70 ATPase activity blocks slow axonal transport and presynaptic accumulation of synapsin.** (A) Schematic of assay to determine slow axonal transport of synapsin using photoactivatable synapsin (PAGFP:synapsin; Roy et al., 2011; Scott et al., 2011). In brief, PAGFP:synapsin was photoactivated in a discrete axonal ROI, and the fluorescence was tracked over time by live imaging. (B) Kymographs from photoactivation experiments in A. Note the anterogradely biased dispersion of PAGFP:synapsin fluorescence in control axons, thought to represent slow transport (midpoint of photoactivated zone marked by red arrowhead and dashed line; top). Also note that the Hsc70 inhibitor (100 μM VER155008; bottom) eliminated the anterograde bias. (C) Quantification of the transport experiments. In brief, the centroid of the photoactivated zone was quantified in each image of a given time-lapse video, and the displacement of the centroid was quantified over time (intensity center shift; Scott et al., 2011). Note that although the population of photoactivated synapsin was transported anterogradely, pharmacologic (VER155008) or genetic (DN-Hsc70) inactivation of Hsc70 ATPase activity prevented the biased transit. (D) Attenuation of endogenous synapsin levels at presynaptic boutons upon selective inactivation of Hsc70 in axons. Axons and presynaptic boutons were isolated from somatodendritic compartments using a triple-chamber microfluidic device (see Fig. S1 for design of device). Thereafter, the Hsc70 inhibitor VER155008 (or DMSO control) was selectively added to the axonal/presynaptic chamber, and the neurons were fixed and immunostained with anti-VAMP2 (to detect all presynapses; green) and anti-synapsin (red) antibodies. Representative images from axonal/presynaptic chambers are shown. (E) Quantification of colocalization between synapsin and VAMP2. Note that Hsc70 inactivation significantly attenuated the presynaptic localization of synapsin. Error bars show means ± SEM. **, P < 0.01.

of Materials and methods; Scott et al., 2011; Tang et al., 2013). Furthermore, to test whether selective inhibition of axonal Hsc70 would also lead to decreased accumulation of synapsin at en passant boutons (after stalling of synapsin transport in axons), we used triple-chambered microfluidic devices where distal axons and boutons can be physically isolated from their somatodendritic counterparts (Fig. S2). Indeed, selective application of the Hsc70 inhibitor to the soma/proximal axons significantly attenuated the targeting of endogenous synapsin to presynaptic boutons, which were physically isolated from the drug (Fig. 6, D and E).

Disruption of axonal synapsin organization upon Hsc70 inactivation

What are the underlying mechanisms by which Hsc70 inactivation attenuates the slow axonal transport of synapsin?

In previous studies, we and others found that overall slow transport is likely a result of dynamic cargo assembly and short-range transport (Scott et al., 2011; Tang et al., 2012, 2013; Twelvetrees et al., 2016)—the dynamic recruitment model (Roy, 2014). Given the established role of Hsc70 in assembling multiprotein complexes, one possibility is that Hsc70 is involved in the proper folding/clustering of synapsin-associated SCb complexes in axons followed by vectorial transit of these complexes. If so, inactivation of Hsc70 ATPase activity would be expected to disrupt these complexes and prevent transport. To test this idea, we first turned to our photoactivation assay, where the rate of fluorescence decay of the photoactivated ROI is a marker of protein mobility (Tang et al., 2013). Specifically, if the photoactivated molecules are more diffusive (i.e., less organized) the decay is expected to be faster. Accordingly, we measured the fluorescence decay of PAGFP:synapsin

in the photoactivated ROI in control axons and in axons where Hsc70 activity was attenuated (Fig. 7 A). As shown in Fig. 7 B, fluorescence decay of PAGFP:synapsin in axons was significantly faster when Hsc70 activity was attenuated.

To test whether the endogenous axonal synapsin puncta (presumably representing transport complexes) were also disrupted upon Hsc70 inactivation, we examined synapsin distribution in axons by immunostaining. As noted previously, endogenous synapsin is punctate in axons, with a low-level diffuse distribution (Fig. 7 C, top; and Fig. S1 A), and these puncta likely represent synapsin–Hsc70 complexes (see DNA-PAINT data; Fig. 5). Interestingly, inhibition of Hsc70 activity led to a disruption of the axonal synapsin distribution. Specifically, the periodic distribution of synapsin puncta was disrupted (Fig. 7 C). Importantly, these effects are not caused by global Hsc70 inactivation, as they were also seen when the Hsc70 inhibitor was selectively applied to axons using microfluidics (Fig. S4, A–C). Note that in VER15508-treated axons, some synapsin puncta are clustered together, whereas other axon segments had few or no synapsin puncta at all. To quantify the disruption of the periodic distribution of synapsin, we performed Fast Fourier transform (FFT) analysis on segments of axons (see details in the Colocalization analysis of widefield images… section of Materials and methods; Zhong et al., 2014) treated with either DMSO (control) or the Hsc70 inhibitor (VER155008). Quantitatively, there was a loss in the periodic frequency of synapsin upon treatment with the Hsc70 inhibitor (loss of major peak) when compared with DMSO (Figs. 7 D and S4 D).

Next, we asked whether inhibition of Hsc70 activity also disrupted the coIP of synapsin–Hsc70 complexes in HEK293 cells (as shown in Fig. 4 D). Accordingly, we performed the coIP experiments with or without adding the Hsc70 inhibitor VER155008. Indeed, inhibition of Hsc70 ATPase significantly decreased the amount of Hsc70 that could be pulled down by synapsin (Fig. 7, E and F), suggesting that Hsc70 activity is involved in consolidating synapsin–Hsc70 complexes. In previous studies, we found that synapsin and other cytosolic proteins cosegregate into higher-density fractions in sucrose gradients from mouse S2 fractions (Scott et al., 2011; Tang et al., 2012). In the context of this paper, Hsc70 and two other chaperones from our proteomics screen (Hsp90 and Cct) also cofractionated with synapsin in higher-density fractions, with subtle changes upon Hsc70 inactivation (Fig. S5). Collectively, the evidence argues for a role of Hsc70 in maintaining physiological organization of synapsin complexes in axons.

Because our previous study shows that slow synapsin transport is dependent on vesicle transport (Tang et al., 2013), we also examined the effects of Hsc70 inhibition on vesicle transport. Previous biochemical studies suggest a physiological role of Hsc70 in motor protein/cytoskeleton regulation (Tsai et al., 2000; Jinwal et al., 2010), though to our knowledge, there have been no live-imaging studies, and the specific effects of Hsc70 inactivation on axonal transport are unknown. We transfected neurons with the pan vesicle marker NPY-ss (Kaech et al., 2012; Das et al., 2016) and examined vesicle transport after both pharmacologic (VER155008) and genetic (Hsc70 D10N mutant) inhibition of Hsc70 activity. We found that Hsc70 inactivation led to the attenuation of vesicle transport (Fig. S3). However, the effects were modest and bidirectional, unlikely to completely account for the block in slow transport seen after Hsc70 inactivation.

Discussion

In this study, we identified proteins associated with synapsin from brain fractions expected to be enriched in cytosolic proteins moving in slow axonal transport. Although a heterogeneous group of proteins was identified, the lists were almost exclusively comprised of cytosolic cargoes, many of which are known to move in SCb. In particular, fractions were enriched in chaperone and cochaperone proteins including Hsc70 (which was also conveyed in slow transport). Interestingly, inactivating the ATPase activity of Hsc70 blocked the slow transport of synapsin, disrupted axonal synapsin complexes, and attenuated Hsc70–synapsin associations. Collectively, the data support a model where inhibition of the Hsc70 ATPase cycle blocks the dynamic clustering of cytosolic molecules and assembly of transient transport complexes.

How are soluble proteins transported?

Individual membrane-anchored proteins are tethered to vesicles, and the latter are transported by molecular motors like kinesins and dyneins (Brady, 1991; Vale, 2003; Fu and Holzbaur, 2014; Maday et al., 2014; Song et al., 2016). However, soluble cytosolic proteins are inherently diffusible, and if these molecules are not organized in some manner, free monomers would simply diffuse inefficiently, and no directional transit would be possible. Visualizing slow axonal transport in living neurons, we and others found that the overall slow movement seems to be generated by dynamic assembly/disassembly of cytosolic molecules into complexes and vectorial transport—the dynamic recruitment model (Scott et al., 2011; Tang et al., 2013; Roy, 2014, 2016; Twelvetrees et al., 2016). A similar biased transport of the enzyme creatine kinase was also seen in squid axons, though particle kinetics have not been resolved in this system (Terada et al., 2000). We reasoned that understanding the composition of transport complexes might offer some clues into the unusual particle kinetics.

The idea that soluble molecules in axons organize into multiprotein transport complexes was proposed in the 1970s and 1980s (Lorenz and Willard, 1978; Tytell et al., 1981; Garner and Lasek, 1982; Scott et al., 2011). Articulated as a part of the overarching structural hypothesis, the idea was that proteins are actively transported in axons as moving structures (Black, 2016). Though conceptually sound, this idea met with much resistance, as many groups failed to find evidence for movement of assembled cytoskeletal structures (Baas and Brown, 1997; Hirokawa et al., 1997). However, more recent studies clearly show that cytoskeletal polymers are transported in axons (Roy et al., 2000; Wang et al., 2000). Relevant to the context of our study, to date there has been little evidence that cytosolic proteins in axons are organized as multiprotein complexes, and the argument for the hypothesis is almost entirely based on biochemical fractionation experiments.

Hsps—potential master regulators of cytosolic slow axonal transport

Hsps are a group of highly conserved proteins that have established roles in the proper folding of nascent polypeptides as well as the formation and stabilization of protein complexes (Bukau et al., 2006; French et al., 2013). Hsc70 is a major constitutively active member of the Hsp family: it is abundant in neurons, has known roles in protein complex assembly and stabilization, and is conveyed in slow axonal transport, as determined by pulse-
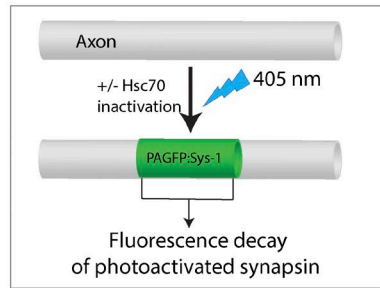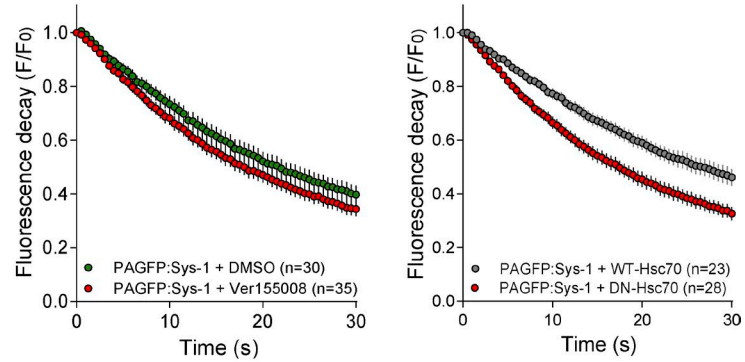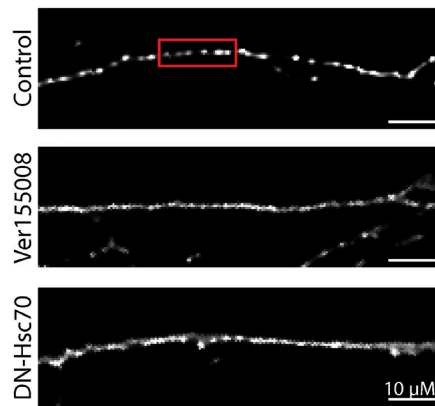
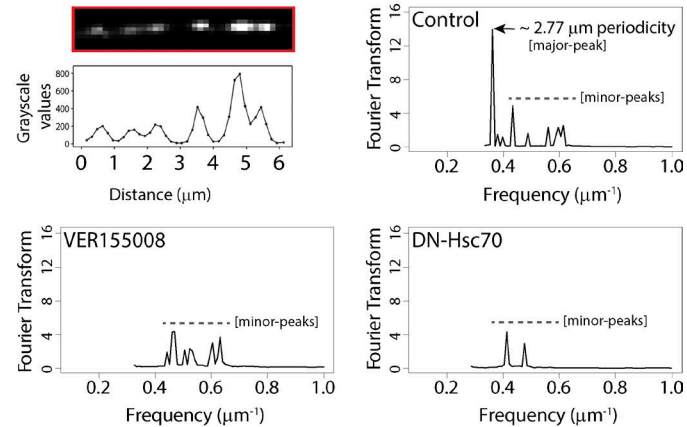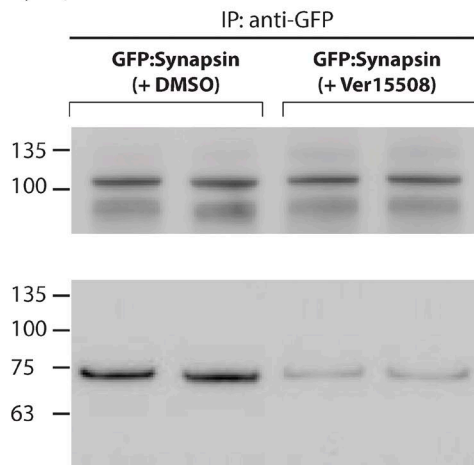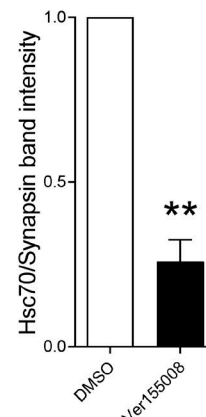Figure 7. **Inactivation of Hsc70 ATPase activity leads to disruption of axonal synapsin.** (A) Strategy to analyze the fluorescence decay of PAGFP:synapsin in an axon ROI over time. PAGFP:synapsin was photoactivated in a discrete axonal ROI, and the dispersion of fluorescence was quantified over time. (B) Fluorescence decay of PAGFP:synapsin in axon ROIs. Note faster decay of fluorescence upon Hsc70 inactivation. (C) Representative images showing endogenous distribution of synapsin in axons upon pharmacologic and genetic Hsc70 inactivation (VER155008 and Hsc70-DN). Note that the punctate distribution is disrupted upon Hsc70 inhibition. (D) Quantification of the periodicity of axonal synapsin particles with or without Hsc70 inactivation. Periodicity of endogenous synapsin particles (i.e., distances between adjacent puncta) was determined from axonal line scans, as shown in the example (top left; red boxed region from C). Cumulative data from control axons is shown on the top right, represented by FFTs (see the Colocalization analysis of widefield images… section of Materials and methods for details). Note the major peak at ~2.77 µm, representing the typical spacing of synapsin puncta in control axons (dashed line over minor peaks). Also note loss of the major peak upon Hsc70 inhibition, reflecting disruption of the periodic synapsin distribution in axons. (E) HEK293 cells were transfected with GFP:synapsin, immunoprecipitated with an anti-GFP antibody, and blotted with anti-GFP and anti-Hsc70 antibodies (with or without VER155008). Note that addition of the Hsc70 inhibitor led to a significant reduction in the amount of immunoprecipitated Hsc70. Molecular mass is shown in kilodaltons. (F) Quantification of blots in E. $n = 3$ separate experiments. Error bars show means ± SEM. **, $P < 0.01$.

chase studies (de Waegh and Brady, 1989; Black et al., 1991). Our coIP/MS data from brains (Figs. 1, 2, 3, and 4), coIP data from HEK cells (Fig. 4 D), and nanometer-resolution view of synapsin–Hsc70 in axons (Fig. 5) argue that synapsin and Hsc70 associate as part of a larger transport complex. In particular, the superresolution data offer a nanometer-resolution view of native SCb complexes and support the notion that synapsin and Hsc70 are part of larger complexes containing other proteins. Moreover, these data suggest that SCb complexes are heterogeneous in size, with estimated mean diameters >100 nm.

Furthermore, our live imaging and immunofluorescence data suggest that the ATPase activity of Hsc70 regulates the organization of synapsin in axons as well as its slow axonal transport. How is this achieved at a molecular level? One possibility is that Hsc70 acts as a scaffold for other SCb molecules, including synapsin, but this seems unlikely, as all Hsc70-induced phenotypes in our study are a result of inhibiting its ATPase activity (and not grossly altering its structure per se). Another possibility is that the ATPase activity of Hsc70 regulates the assembly and/or organization of synapsin transport complexes, a view supported by the data in Fig. 7, where Hsc70 inhibition led to a disruption of axonal synapsin puncta, which presumably represent synapsin complexes. How might Hsc70 regulate synapsin transport at a molecular level? Available data suggest that ADP-bound Hsc70 has a higher affinity for its substrates than ATP-bound Hsc70 (Bukau et al., 2006). One can imagine a scenario where synapsin and other cytosolic peptides moving in SCb dynamically associate with Hsc70, and inhibition of the ATPase cycle prevents Hsc70 from tethering to—and clustering—SCb proteins, thus disrupting the organization of SCb cargoes and consequently, the slow transport of protein complexes. Because Hsc70 is also conveyed in slow transport, it is well situated to play such a regulatory role. Speculatively, Hsc70-dependent consolidation into supramolecular complexes would be expected to inhibit degradation of soluble proteins, and this might also explain the paradox between the prolonged transit of these proteins in slow transport in pulse-chase studies (over days) and their known short half-lives (typically hours at synapses, where turnover has been studied; Cohen et al., 2013). However, testing of these scenarios would require further dissection of SCb complexes and intramolecular associations.

Caveats and summary

The main caveat in our experiments is that our starting material for the MS experiments may not be exclusively comprised of the transported SCb fraction. Though the axonally transported cargoes are expected to be present in synaptosome-depleted samples (Scott et al., 2011; Twelvetrees et al., 2016), the latter may also contain synapsin-associated proteins that are not involved in the transport process. An exclusive examination of the transported cargo would require selective labeling of the moving fraction and determining the peptide composition therein. Unfortunately, available model systems to evaluate overall slow transport are based on radioactive labeling, and it is not practical to combine these with MS. Moreover, though the sensitivity of MudPIT-MS is high, getting enough starting material for high-confidence analyses is still a limitation in coIP/MS experiments. Nevertheless, our superresolution imaging shows axonal synapsin–Hsc70 coclusters all along the axon, suggesting that perhaps most of these complexes are transport competent. Moreover, we note that unbiased MS experiments led us to Hsc70, which biochemically associates with synapsin and

seems to have a role in soluble slow axonal transport. Given the links between fast and slow transport, the attenuation of vesicle transport after Hsc70 inactivation (Fig. S3) might also influence synapsin transport. Future studies parsing the effects of Hsc70 on fast and slow transport may provide clarity. The exact nature of synapsin–Hsc70 associations remains unclear. In coIP experiments using HEK cells (Fig. 4 D), we cannot rule out the possibility of nonspecific interactions caused by synapsin overexpression. Also, although our experiments strongly suggest that Hsc70 acts locally in axons, most experiments were performed after global inhibition of Hsc70 ATPase activity. Thus, it remains possible that Hsc70 may also play a role in cargo sorting within the soma before export into axons.

Though the idea that soluble proteins associate into multiprotein transport complexes was articulated several decades ago, until now there have been no systematic efforts to evaluate the proteome of slow transport. Our study provides an inventory of such complexes and also implicate Hsps as potential regulators of slow axonal transport. We hope that the insights from our experiments will serve as a starting point for future studies probing this enigmatic rate class.

Materials and methods

Cell culture, transfections, plasmids, and inhibitors

Hippocampal cultures were obtained from brains of postnatal (P0–P2) CD-1 mice (either sex) and maintained in accordance with University of California guidelines as described previously (Roy et al., 2011; Ganguly and Roy, 2014; Ganguly et al., 2015). Neurons were transfected with the appropriate fluorescent constructs at 7–9 d in vitro (DIV) with Lipofectamine 2000 (Invitrogen) and allowed to express for 14–16 h after transfection. 1.2 µg of DNA was added to every 5 ml of the transfection mixture for all the constructs used in the study, unless otherwise mentioned. The Hsc70-D10N constructs were from N. Lamarche-Vane (McGill University, Montreal, Canada), and the NPY-ss:mCherry constructs were from G. Banker (University of Oregon, Eugene, OR). Synapsin deletion mutant constructs were described previously by Gitler et al. (2004b). The GFP:synapsin-Ia and soluble mCherry constructs were subcloned into the PAGFP vector by using standard cloning techniques. All constructs used in this study were confirmed by sequencing. VER155008 was used as the Hsc70 inhibitor (3803; Tocris Bioscience). This drug was dissolved in DMSO and used at a working concentration of 100 µM. Drug was incubated with neuronal cultures for 12–16 h overnight after transfection.

Biochemical fractionation and IP from mouse whole brain

In vivo biochemical assays were adapted from the protocol described previously by Scott et al. (2011) and Tang et al. (2012). In brief, 4–6-wk-old mouse brains (5 g of total tissue for each genotype) from CD-1 (WT) and synapsin TKO mice were homogenized in nondenaturing buffer containing 20 mM Hepes, pH 7.2, 40 mM KCl, 5 mM EGTA, 5 mM EDTA, and protease inhibitors. The resulting homogenate was centrifuged at 1,000 g for 20 min to obtain a nuclear pellet (P1) and a postnuclear supernatant (S1). The S1 supernatant was then centrifuged at 10,200 g for 20 min to obtain a crude synaptosomal fraction (P2) and synaptosome-depleted fraction (S2). S2 supernatant was further centrifuged at 100,000 g for 1 h at 4°C to obtain the S100 supernatant and the pellet fraction (P100) in a SW55-T*i* rotor fitted in an Optima L-100 ultracentrifuge (Beckman Coulter).

IP was performed using the DynaBeads Co-Immunoprecipitation kit (14321D; Thermo Fisher Scientific). After centrifugation, each

fraction was divided equally and incubated with 7 mg anti–Synapsin-I antibody (106001; Synaptic Systems) for overnight coupling with magnetic beads at 37°C (DynaBeads; Invitrogen). All following washes were performed as per the manufacturer's protocol. Lysate fractions were incubated with the antibody-coupled beads for 30 min at 4°C on a rotor. After the final wash, 1.5 mg beads from each fraction were subjected to 2D gel electrophoresis on a native page gel and then subjected to silver staining (Pierce Silver Stain kit; 24612; Thermo Fisher Scientific). The remaining 5.5 mg beads from each fraction were then subjected to MudPIT-MS analysis. Three independent repeats were performed with WT brain lysate fractions, whereas two were performed with the Synapsin TKO brain lysate.

Protein identification through MudPIT-MS analysis

100 µl of 8 M urea in 100 mM Tris, pH 8.5, was added to the beads for each fraction, followed by reduction and alkylation in 10 mM Tris (2-carboxyethyl)phosphine hydrochloride (Roche) and 55 mM iodo-acetamide (Sigma-Aldrich), respectively. The sample was then diluted fourfold by the addition of 100 mM Tris-HCl, pH 8.5, followed by digestion in trypsin (Promega; incubated at 37°C overnight in the dark). Magnetic beads in the sample were then removed by a magnetic separator. The resulting protein digest was acidified with formic acid (final concentration 5%) followed by centrifugation at 14,000 rpm for 10 min. Thereafter, the supernatant was pressure loaded onto a 250 µm inner diameter–fused silica capillary column (Polymicro Technologies). This column was fitted with a Kasil frit packed with 2.5 cm of 5-µm Partisphere strong cation exchange resin (Whatman) and 2.5 cm of 5-µm C18 resin (Phenomenex). After desalting, this biphasic column was connected to a 100-µm inner diameter–fused silica capillary (Polymicro Technologies) analytical column with a 3-µm pulled tip packed with 10 cm of 3-µm C18 resin (Phenomenex). The entire three-phase column was then laced in line with a 1,200 quaternary HPLC pump (Agilent Technologies) and analyzed using a modified 12-step separation described previously (Washburn et al., 2001). As peptides were eluted from the microcapillary column, they were electrosprayed directly into a hybrid LTQ Orbitrap Velos mass spectrometer (Thermo Fisher Scientific). A cycle consisted of one full-scan mass spectrum (300–1,600 m/z) followed by 20 data-dependent collision-induced dissociation tandem MS spectra. The application of mass spectrometer scan functions and HPLC solvent gradients was controlled by the Xcalibur data system (Thermo Fisher Scientific). Tandem MS spectra were extracted using RawXtract (version 1.9.9; McDonald et al., 2004) and searched with the ProLuCID algorithm (Xu et al., 2015) against a mouse UniProt database concatenated to a decoy database in which the sequence for each entry in the original database was reversed (Peng et al., 2003). The ProLuCID search was performed using semienzyme specificity and static modification of cysteine because of carboxyamidomethylation (57.02146). ProLuCID search results were assembled and filtered using the DTASelect algorithm (version 2.0; Tabb et al., 2002). The protein identification false positive rate was kept below 1%, and all peptide–spectra matches had <10 ppm mass error.

Biochemical analysis of the effect of Hsc70 inhibition on mouse brain tissue

Sequential isolation and density gradient centrifugation were performed to fractionate the soluble cytosolic fractions as described previously (Scott et al., 2011; Das et al., 2013). In brief, brains from 6–8-wk-old CD-1 mice were homogenized in buffer containing 20 mM Hepes, 40 mM KCl, 5 mM EDTA, 5 mM EGTA, and protease inhibitor, pH 7.2, either in the presence of 1 mM Hsc70 inhibitor (VER155008) or DMSO (control lysate). Tissue lysate was centrifuged at 1,000 g for 15 min to isolate after nuclear supernatant (S1). S1 was centrifuged

at 10,200 g for 20 min to obtain synaptosome-depleted fraction (S2). The S2 fraction was then centrifuged at 100,000 g for 1 h at 4°C to isolate soluble (S100) and vesicular (P100) fractions. The S100 lysate was incubated at 37°C for 4 h before performing the density gradient floatation assay. For the density gradient floatation assay, S100 fractions were adjusted to 45% sucrose, bottom loaded on a 5–45% sucrose gradient, and centrifuged at 160,000 g for 16 h at 4°C in a SW55-Ti rotor in an Optima L-100 ultracentrifuge. 10 fractions of 0.5 ml each were collected from the top of the gradient column, and equal volumes were used for SDS-PAGE and Western blot analysis. Anti–Synapsin-I, anti-Hsc70 (ab19136; Abcam), anti-Hsp90 (4877; Cell Signaling Technology), and anti-Cct2 (3561; Cell Signaling Technology) primary antibodies were used at 1:1,000 dilution to probe the blot. Blots were developed by using Fast Western Blot kit ECL Substrate (Thermo Fisher Scientific) and visualized by using Versa Doc Imaging system (Bio-Rad Laboratories). For experiments with VER15508, the inhibitor was present at every step of the process.

Protein selection and in silico data analysis

To normalize datasets from various runs, spectrum counts of each detected peptide in a given run were divided by the total spectrum count of all peptides detected in that run. Normalized spectrum counts from the various runs were averaged to obtain the final spectrum count for WT and TKO groups (French et al., 2013). Two-tier inclusion criteria were applied (also see schematic in Fig. 2). First, peptides with final counts of 0 in the TKO lysate and >0 in the WT lysate were selected. Second, peptides with spectral counts twofold or more in the WT lysate (as compared with TKO) were selected. All peptides that meet either or both criteria were included in the final list. Three such peptide lists were generated from the P2, P100, and S100 fractions. For functional grouping of peptides based on molecular function, gene names were entered in the Panther database (http://www.pantherdb.org) and sorted based on known molecular function. For generation of the interaction map of various chaperones detected in the S100 fraction, all known interactions from experimental data were determined from the String protein interaction database (http://www.string-db.org). Interactions between the identified genes was manually added using the Osprey network visualization software (http://biodata.mshri.on.ca/osprey/servlet/Index).

Microscopy, live imaging/analysis, and synaptic targeting

The photoactivation and live-imaging experiments were performed using an inverted motorized epifluorescence microscope (IX81; Olympus) equipped with CoolSNAP HQ² camera (Photometrics). Details of the photoactivation setup were described previously (Roy et al., 2011). In brief, a dual-source light illuminator (IX2-RFAW; Olympus) was used to simultaneously visualize and photoactivate a discrete ROI within the axon. Kymographs were generated using dropdown menus in MetaMorph (version 7.7; Molecular Devices). Immediately before live imaging, neurons were transferred to Hibernate media (Brainbits) supplemented with 2% B27, 2 mM Glutamax, 0.4% ᴅ-glucose, and 37.5 mM NaCl (Roy et al., 2011; Scott et al., 2011), and maintained at 37°C (Precision Control Weatherstation) for the duration of the experiments. Axons were identified based on morphology, and only neurons with unambiguous morphology were selected for imaging (Roy et al., 2011; Scott et al., 2011). For photoactivation experiments, PAGFP:synapsin was photoactivated for 1 s and imaged at two frames per second with a 100× oil immersion lens unless otherwise stated. NPY-ss–mCherry transport was performed using the stream acquisition function of MetaMorph at five frames per second for 30 s with a 200-ms continuous exposure (with no time interval between images). The field diaphragm was closed down to expose only the part of the axon being imaged and also to minimize photobleaching.

To analyze the transport of synapsin, the intensity-center assay was performed using algorithms written in MATLAB (MathWorks; Roy et al., 2011; Scott et al., 2011). In brief, after photoactivation and time-lapse imaging, the videos were background-subtracted, and the photoactivated ROI was cropped. Intensity line scans along the axon were generated for each frame in the video, and the maximum intensity point (intensity center) was calculated. Shifts in the fluorescence population resulted in a corresponding shift of the intensity center as well, and these were numerically plotted in Prism (GraphPad Software) for display. Fast transport of NPY-ss–mCherry kymographs from each 16-bit video file were generated using the Kymograph function in MetaMorph Image Analysis software blinded for each condition and analyzed manually. All data were plotted in Prism for display. For synaptic targeting experiments (Fig. 6 D), cultured DIV 13 neurons were cotransfected with GFP:synapsin and mCherry:Hsc70-D10N (or soluble mCherry). Live-cell imaging was performed 16 h after transfection as described previously (Wang et al., 2014). In brief, Z stack images were obtained with 0.339-µm step size, and all images were acquired, processed, and analyzed using MetaMorph software. All statistical analyses were performed using Prism software.

Superresolution imaging of endogenous synapsin and Hsc70 in axons and image analyses

Rat hippocampal neurons (from E18 pups) were cultured on 18-mm coverslips at a density of 6,000/cm² following the established guidelines of the European Animal Care and Use Committee (86/609/CEE) and the approval of the local ethics committee (agreement D13-055-8). Axons of DIV 7–9 neurons were identified by labeling of the axon initial segment with an antibody against an extracellular epitope of neurofascin-186 (monoclonal mouse anti-NF186 clone A12/18; NeuroMAB; Schafer et al., 2009). Neurons were then fixed using 4% PFA in PEM (80 mM Pipes, 5 mM EGTA, and 2 mM MgCl₂, pH 6.8) for 10 min. After blocking, neurons were incubated with anti–synapsin-I (AB1543; EMD Millipore) and anti-Hsc70 (ab2788; Abcam) primary antibodies overnight at 4°C, then with DNA-conjugated secondary antibodies (Ultivue) for 1 h at RT. DNA-PAINT imaging (Jungmann et al., 2014) was performed on an N-STORM microscope (Nikon). Coverslips were imaged in imaging buffer with 0.32 nM Imager-650 and 0.16 nM Imager-560 (Ultivue). The sample was alternatively illuminated at 647 and 561 nm (full laser power), and 20,000-30,000 images of each channel were acquired at 25–33 Hz.

Objects in superresolution images were analyzed in two overall steps using the image processing package Fiji (Version 2.0.0-rc-54/1.51h; ImageJ; National Institutes of Health) and RStudio (Version 1.0.44; running R version 3.3.2). Objects were first thresholded using the "IsoData" automatic thresholding algorithm in Fiji. To obtain meaningful quantitative data from irregularly shaped objects in the images, individual particles were subjected to a 0.4–1.0 circularity constraint, where 1.0 and 0.0 represented complete circularity and complete irregularity, respectively, which was a constraint that captured most particles. Various parameters were then calculated, including area, intensity center of mass (based on intensity variations within each particle), and bounding rectangle dimensions (the diagonals of the bounding rectangle were used to represent particle diameters). Subsequent analyses on this filtered population were done in RStudio. First, outliers in the filtered images were excluded from analyses using a predefined upper and lower bound area (anything above and below 300 pixels and 10 pixels, respectively). Thereafter, proximity of the centers of mass of synapsin and Hsc70 particles was determined. Specifically, particles of one condition were defined as proximal to the other if the distances between their respective centers of mass fell below a fixed, user-defined threshold distance (Fig. 5, D and E).

IPs and immunoblotting of HEK293T cell lysate

HEK293T cells were transfected with various full-length and truncated GFP–tagged synapsin constructs (Gitler et al., 2004b). Soluble GFP was the control vector. HEK293T (1 d after transfection) homogenates were solubilized in 1×IP buffer (Invitrogen) supplemented with protease inhibitors at 4°C. After centrifugation at 16,000 g for 10 min at 4°C, the clarified lysate was subjected to IPs with GFP antibody (ab290; Abcam) and 50 µl of magnetic protein G beads (Invitrogen) for 2 h at 4°C. After three washes with 1 ml of the IP buffer, bound proteins were eluted with 2× SDS sample buffer containing 10% β-mercaptoethanol and boiled for 10 min at 100°C. Coprecipitated proteins were separated by SDS-PAGE and transferred onto PVDF membranes. Blots were blocked in PBS containing 0.5% Tween-20 and 5% fat-free milk for 30 min at RT. The blocked membrane was incubated in blocking buffer containing primary antibody overnight at 4°C followed by three washes. The washed membrane was incubated in blocking buffer containing HRP-conjugated secondary antibody (1:2,000; Invitrogen) for 2 h at RT. HRP immunoblots were developed using an ECL Western blotting substrate (Thermo Fisher Scientific). Primary antibodies used were GFP antibody (1:5,000; ab290; Abcam) and Hsc70 antibody (1:1,000). For experiments with VER15508, 50 µM of the drug was added to cells for 12 h, and the inhibitor was also included in all buffers during IP.

Immunohistochemistry and colocalization analysis

Immunohistochemistry. For immunostaining of endogenous synapsin and Hsc70 DIV 6–7 neurons were fixed in 4% PFA/sucrose solution in PBS for 10 min at RT, extracted in PBS containing 0.2% Triton X-100 for 10 min at RT, blocked for 2 h at RT in 1% bovine serum albumin and 5% FBS, and then incubated with 1:1,000 mouse anti–synapsin-I and 1:500 rat anti-Hsc70 diluted in PBS for 2 h at RT. After removal of primary antibody, neurons were blocked for 30 min at RT, incubated with goat anti–mouse (Alexa Fluor 488) and goat anti–rat secondary antibody (Alexa Fluor 594) at 1:1,500 dilution for 1 h at RT and then mounted for imaging. Images were acquired using an inverted epifluorescence microscope (Eclipse T*i*-E) equipped with CFI S Fluor VC 40× NA 1.30 and CFI Plan Apochromat VC 100× NA 1.40 oil objectives (Nikon). An electron-multiplying charge-coupled device camera (QuantEM: 512SC; Photometrics) and LED illuminator (SPECTRA X; Lumencor) were used for all image acquisition. The system was controlled by Elements software (NIS Elements Advanced Research 64 bit; 4.13.00; Nikon). All images were converted to 16-bit TIFF files for analysis in Metamorph.

Preparation of microfluidic chambers for immunostaining. Triple-chambered microfluidic devices with a 500-µm central chamber (TCND500; Xona Microfluidics) were washed in 100% ethanol, air dried, and sterilized for 15 min under UV light before use. The sterile device was placed on a 24 × 60 mm rectangular coverslip, which was coated with 1 mg/ml Poly-ᴅ-lysine for 4 h at RT, washed twice with double distilled H₂O, and then air dried before the device was placed on it. A tight seal between the device and the coverslip was ensured by the application of manual pressure. Hippocampal neurons were plated at a density of 2.0–2.5 × 10⁵ cells/µl in chambers of a triple-chambered microfluidic device (see Figs. S2 and S4 for layout). 150 µl of plating media was added to each pair of wells (top and bottom) connecting each chamber after plating the neurons. To maintain a fluidic gradient between chambers, a 50-µl volume difference was maintained between the top and bottom wells connecting each chamber. Before fixation, for Fig. S4 C, 100 µM VER155008 (4–6 h) or DMSO was added only to chamber A (see Fig. S2 A) of the microfluidic device, whereas for Fig. 7 E, drug/DMSO was added only to chamber B of the device. Immunostaining was done as described previously (Scott et al., 2011; Tang et al., 2012). The anti-synaptobrevin2 (VAMP2) antibody

(104011; Synaptic Systems) was used to mark presynaptic boutons, whereas β-tubulin (PRB-435P; Covance) was used to mark axons.

Colocalization analysis of widefield images

To quantify the proximity of endogenous synapsin and Hsc70 puncta in axons, we developed algorithms that considered two particles to be colocalized if they were within 2 pixels (0.32 µm) of each other. Specifically, line scans were drawn on synapsin- and Hsc70-stained axons, peak fluorescence values for synapsin–Hsc70 puncta were obtained, and the peaks were then normalized and compared as detailed below.

Derivative peak detection analysis. For each image, a line scan was performed on an ROI in an axon using MetaMorph Imaging Software, and the fluorescence intensity profile over space was obtained as a set of coordinates. These coordinates were fed into a script written in R (Version 3.2.2), and an interpolation function was created from the set of coordinates. The derivative of the interpolation function was computed, and a set of coordinates corresponding to the derivative function was obtained. These coordinates were then scanned to determine points at which the function takes on positive values, hits zero, and returns to negative values with a significant difference that exceeds a set threshold. The values that meet these criteria were determined as peaks corresponding to protein locations and were recorded. The distances between these detected peaks were then determined and averaged, representing the distances between the proteins in the condition of interest. This analysis was performed for both the synapsin and Hsc70 images.

FFT analysis. For each image, a fluorescence intensity profile over space for each axon ROI was produced similar to the derivative peak detection analysis described in the previous section. All the following processes were performed in R. An FFT analysis was performed on the values for the amplitude of the intensity profile obtained. These values were then plotted against frequency values, which were obtained by performing the following normalization on the distance coordinates

$$F_{fft} = \frac{S_f * x}{N_{fft}}.$$

F_{fft} is the vector of frequency values, S_f is the sampling frequency, N_{fft} is the length of the FFT values, and x is the vector of distance values obtained from the fluorescence intensity profile. An interpolating function was created using the FFT values and the F_{fft} values. The derivative peak detection analysis described in the previous section was performed on the interpolating function, yielding the peak frequencies of the protein distribution in µm^{-1}. All images for each condition were processed as described here, and the mean frequencies were determined for each condition. The inverses of the frequencies were then used to determine the mean periodicities in µm and were compared across conditions.

Online supplemental material

Fig. S1. shows endogenous synapsin and Hsc70 distribution in cultured hippocampal neurons. Fig. S2 shows a microfluidic device to examine presynaptic boutons. Fig. S3 shows the effects of Hsc70 ATPase inhibition on fast vesicle transport. Fig. S4 shows disruption of axonal synapsin upon Hsc70 inhibition in isolated axons. Fig. S5 shows density gradients of S100 fractions from mouse brains blotted with synapsin and members of the Hsp family pulled down by our proteomics screen (Hsc70, Hsp90, and Cct2). Table S1 is a list of P2 fractions. Table S2 is a list of S100 fractions. Table S3 is a list of P100 fractions. Table S4 is a list of synapsin interactors from literature found in P100 + S100 fractions.

References

Baas, P.W., and A. Brown. 1997. Slow axonal transport: the polymer transport model. *Trends Cell Biol.* 7:380–384. http://dx.doi.org/10.1016/S0962 -8924(97)01148-3

Baitinger, C., and M. Willard. 1987. Axonal transport of synapsin I-like proteins in rabbit retinal ganglion cells. *J. Neurosci.* 7:3723–3735.

Black, M.M. 2016. Axonal transport: The orderly motion of axonal structures. *Methods Cell Biol.* 131:1–19. http://dx.doi.org/10.1016/bs.mcb.2015.06 .001

Black, M.M., and R.J. Lasek. 1979. Axonal transport of actin: Slow component b is the principal source of actin for the axon. *Brain Res.* 171:401–413. http ://dx.doi.org/10.1016/0006-8993(79)91045-X

Black, M.M., and R.J. Lasek. 1980. Slow components of axonal transport: two cytoskeletal networks. *J. Cell Biol.* 86:616–623. http://dx.doi.org/10 .1083/jcb.86.2.616

Black, M.M., M.H. Chestnut, I.T. Pleasure, and J.H. Keen. 1991. Stable clathrin: uncoating protein (hsc70) complexes in intact neurons and their axonal transport. *J. Neurosci.* 11:1163–1172.

Bourke, G.J., W. El Alami, S.J. Wilson, A. Yuan, A. Roobol, and M.J. Carden. 2002. Slow axonal transport of the cytosolic chaperonin CCT with Hsc73 and actin in motor neurons. *J. Neurosci. Res.* 68:29–35. http://dx.doi.org /10.1002/jnr.10186

Brady, S.T. 1991. Molecular motors in the nervous system. *Neuron.* 7:521–533. http://dx.doi.org/10.1016/0896-6273(91)90365-7

Brady, S.T., M. Tytell, K. Heriot, and R.J. Lasek. 1981. Axonal transport of calmodulin: a physiologic approach to identification of long-term associations between proteins. *J. Cell Biol.* 89:607–614. http://dx.doi.org /10.1083/jcb.89.3.607

Bukau, B., and A.L. Horwich. 1998. The Hsp70 and Hsp60 chaperone machines. *Cell.* 92:351–366. http://dx.doi.org/10.1016/S0092-8674(00)80928-9

Bukau, B., J. Weissman, and A. Horwich. 2006. Molecular chaperones and protein quality control. *Cell.* 125:443–451. http://dx.doi.org/10.1016/j .cell.2006.04.014

Cesca, F., P. Baldelli, F. Valtorta, and F. Benfenati. 2010. The synapsins: Key actors of synapse function and plasticity. *Prog. Neurobiol.* 91:313–348. http://dx.doi.org/10.1016/j.pneurobio.2010.04.006

Clark, B.D., and I.R. Brown. 1985. Axonal transport of a heat shock protein in the rabbit visual system. *Proc. Natl. Acad. Sci. USA.* 82:1281–1285. http ://dx.doi.org/10.1073/pnas.82.4.1281

Cohen, L.D., R. Zuchman, O. Sorokina, A. Müller, D.C. Dieterich, J.D. Armstrong, T. Ziv, and N.E. Ziv. 2013. Metabolic turnover of synaptic proteins: Kinetics, interdependencies and implications for synaptic maintenance. *PLoS One.* 8:e63191. http://dx.doi.org/10.1371/ journal.pone.0063191

Collins, M.O., L. Yu, M.P. Coba, H. Husi, I. Campuzano, W.P. Blackstock, J.S. Choudhary, and S.G. Grant. 2005. Proteomic analysis of in vivo phosphorylated synaptic proteins. *J. Biol. Chem.* 280:5972–5982. http:// dx.doi.org/10.1074/jbc.M411220200

Das, U., D.A. Scott, A. Ganguly, E.H. Koo, Y. Tang, and S. Roy. 2013. Activity-induced convergence of APP and BACE-1 in acidic microdomains via an endocytosis-dependent pathway. *Neuron.* 79:447–460. http://dx.doi.org /10.1016/j.neuron.2013.05.035

Das, U., L. Wang, A. Ganguly, J.M. Saikia, S.L. Wagner, E.H. Koo, and S. Roy. 2016. Visualizing APP and BACE-1 approximation in neurons yields insight into the amyloidogenic pathway. *Nat. Neurosci.* 19:55–64. http:// dx.doi.org/10.1038/nn.4188

DeGeer, J., A. Kaplan, P. Mattar, M. Morabito, U. Stochaj, T.E. Kennedy, A. Debant, M. Cayouette, A.E. Fournier, and N. Lamarche-Vane. 2015. Hsc70 chaperone activity underlies Trio GEF function in axon growth and guidance induced by netrin-1. *J. Cell Biol.* 210:817–832. http://dx .doi.org/10.1083/jcb.201505084

de Waegh, S., and S.T. Brady. 1989. Axonal transport of a clathrin uncoating ATPase (HSC70): A role for HSC70 in the modulation of coated vesicle assembly in vivo. *J. Neurosci. Res.* 23:433–440. http://dx.doi.org/10.1002/jnr.490230409

Dillman, J.F. III, L.P. Dabney, S. Karki, B.M. Paschal, E.L. Holzbaur, and K.K. Pfister. 1996. Functional analysis of dynactin and cytoplasmic dynein in slow axonal transport. *J. Neurosci.* 16:6742–6752.

French, J.B., H. Zhao, S. An, S. Niessen, Y. Deng, B.F. Cravatt, and S.J. Benkovic. 2013. Hsp70/Hsp90 chaperone machinery is involved in the assembly of the purinosome. *Proc. Natl. Acad. Sci. USA.* 110:2528–2533. http://dx.doi.org/10.1073/pnas.1300173110

Fu, M.M., and E.L. Holzbaur. 2014. Integrated regulation of motor-driven organelle transport by scaffolding proteins. *Trends Cell Biol.* 24:564–574. http://dx.doi.org/10.1016/j.tcb.2014.05.002

Ganguly, A., and S. Roy. 2014. Using photoactivatable GFP to track axonal transport kinetics. *Methods Mol. Biol.* 1148:203–215. http://dx.doi.org/10.1007/978-1-4939-0470-9_13

Ganguly, A., Y. Tang, L. Wang, K. Ladt, J. Loi, B. Dargent, C. Leterrier, and S. Roy. 2015. A dynamic formin-dependent deep F-actin network in axons. *J. Cell Biol.* 210:401–417. http://dx.doi.org/10.1083/jcb.201506110

Garner, J.A., and R.J. Lasek. 1981. Clathrin is axonally transported as part of slow component b: the microfilament complex. *J. Cell Biol.* 88:172–178. http://dx.doi.org/10.1083/jcb.88.1.172

Garner, J.A., and R.J. Lasek. 1982. Cohesive axonal transport of the slow component b complex of polypeptides. *J. Neurosci.* 2:1824–1835.

Giovedí, S., A. Corradi, A. Fassio, and F. Benfenati. 2014. Involvement of synaptic genes in the pathogenesis of autism spectrum disorders: the case of synapsins. *Front Pediatr.* 2:94.

Gitler, D., Y. Takagishi, J. Feng, Y. Ren, R.M. Rodriguiz, W.C. Wetsel, P. Greengard, and G.J. Augustine. 2004a. Different presynaptic roles of synapsins at excitatory and inhibitory synapses. *J. Neurosci.* 24:11368–11380. http://dx.doi.org/10.1523/JNEUROSCI.3795-04.2004

Gitler, D., Y. Xu, H.T. Kao, D. Lin, S. Lim, J. Feng, P. Greengard, and G.J. Augustine. 2004b. Molecular determinants of synapsin targeting to presynaptic terminals. *J. Neurosci.* 24:3711–3720. http://dx.doi.org/10.1523/JNEUROSCI.5225-03.2004

Grafstein, B., and D.S. Forman. 1980. Intracellular transport in neurons. *Physiol. Rev.* 60:1167–1283.

Hirokawa, N., S.T. Funakoshi, and S. Takeda. 1997. Slow axonal transport: the subunit transport model. *Trends Cell Biol.* 7:384–388. http://dx.doi.org/10.1016/S0962-8924(97)01133-1

Huang, S.P., M.Y. Tsai, Y.M. Tzou, W.G. Wu, and C. Wang. 1993. Aspartyl residue 10 is essential for ATPase activity of rat hsc70. *J. Biol. Chem.* 268:2063–2068.

Jinwal, U.K., J.C. O'Leary III, S.I. Borysov, J.R. Jones, Q. Li, J. Koren III, J.F. Abisambra, G.D. Vestal, L.Y. Lawson, A.G. Johnson, et al. 2010. Hsc70 rapidly engages tau after microtubule destabilization. *J. Biol. Chem.* 285:16798–16805. http://dx.doi.org/10.1074/jbc.M110.113753

Jungmann, R., M.S. Avendaño, J.B. Woehrstein, M. Dai, W.M. Shih, and P. Yin. 2014. Multiplexed 3D cellular super-resolution imaging with DNA-PAINT and Exchange-PAINT. *Nat. Methods.* 11:313–318. http://dx.doi.org/10.1038/nmeth.2835

Kaech, S., C.F. Huang, and G. Banker. 2012. Short-term high-resolution imaging of developing hippocampal neurons in culture. *Cold Spring Harb. Protoc.* 2012:340–343.

Koike, H., and H. Matsumoto. 1985. Fast axonal transport of membrane protein and intra-axonal diffusion of free leucine in a neuron of *Aplysia*. *Neurosci. Res.* 2:281–285. http://dx.doi.org/10.1016/0168-0102(85)90006-9

Lasek, R.J., J.A. Garner, and S.T. Brady. 1984. Axonal transport of the cytoplasmic matrix. *J. Cell Biol.* 99:212s–221s. http://dx.doi.org/10.1083/jcb.99.1.212s

Lorenz, T., and M. Willard. 1978. Subcellular fractionation of intra-axonally transport polypeptides in the rabbit visual system. *Proc. Natl. Acad. Sci. USA.* 75:505–509. http://dx.doi.org/10.1073/pnas.75.1.505

Maday, S., A.E. Twelvetrees, A.J. Moughamian, and E.L. Holzbaur. 2014. Axonal transport: Cargo-specific mechanisms of motility and regulation. *Neuron.* 84:292–309. http://dx.doi.org/10.1016/j.neuron.2014.10.019

Massey, A.J., D.S. Williamson, H. Browne, J.B. Murray, P. Dokurno, T. Shaw, A.T. Macias, Z. Daniels, S. Geoffroy, M. Dopson, et al. 2010. A novel, small molecule inhibitor of Hsc70/Hsp70 potentiates Hsp90 inhibitor induced apoptosis in HCT116 colon carcinoma cells. *Cancer Chemother. Pharmacol.* 66:535–545. http://dx.doi.org/10.1007/s00280-009-1194-3

McDonald, W.H., D.L. Tabb, R.G. Sadygov, M.J. MacCoss, J. Venable, J. Graumann, J.R. Johnson, D. Cociorva, and J.R. Yates III. 2004. MS1, MS2, and SQT—three unified, compact, and easily parsed file formats for the storage of shotgun proteomic spectra and identifications. *Rapid Commun. Mass Spectrom.* 18:2162–2168. http://dx.doi.org/10.1002/rcm.1603

Mills, R.G., L.S. Minamide, A. Yuan, J.R. Bamburg, and J.J. Bray. 1996. Slow axonal transport of soluble actin with actin depolymerizing factor, cofilin, and profilin suggests actin moves in an unassembled form. *J. Neurochem.* 67:1225–1234. http://dx.doi.org/10.1046/j.1471-4159.1996.67031225.x

Paggi, P., and T.C. Petrucci. 1992. Neuronal compartments and axonal transport of synapsin I. *Mol. Neurobiol.* 6:239–251. http://dx.doi.org/10.1007/BF02780556

Peng, J., J.E. Elias, C.C. Thoreen, L.J. Licklider, and S.P. Gygi. 2003. Evaluation of multidimensional chromatography coupled with tandem mass spectrometry (LC/LC-MS/MS) for large-scale protein analysis: The yeast proteome. *J. Proteome Res.* 2:43–50. http://dx.doi.org/10.1021/pr025556v

Peng, J., M.J. Kim, D. Cheng, D.M. Duong, S.P. Gygi, and M. Sheng. 2004. Semiquantitative proteomic analysis of rat forebrain postsynaptic density fractions by mass spectrometry. *J. Biol. Chem.* 279:21003–21011. http://dx.doi.org/10.1074/jbc.M400103200

Roy, S. 2014. Seeing the unseen: The hidden world of slow axonal transport. *Neuroscientist.* 20:71–81. http://dx.doi.org/10.1177/1073858413498306

Roy, S. 2016. Dynein's life in the slow lane. *Neuron.* 90:907–909. http://dx.doi.org/10.1016/j.neuron.2016.05.026

Roy, S., P. Coffee, G. Smith, R.K. Liem, S.T. Brady, and M.M. Black. 2000. Neurofilaments are transported rapidly but intermittently in axons: Implications for slow axonal transport. *J. Neurosci.* 20:6849–6861.

Roy, S., G. Yang, Y. Tang, and D.A. Scott. 2011. A simple photoactivation and image analysis module for visualizing and analyzing axonal transport with high temporal resolution. *Nat. Protoc.* 7:62–68. http://dx.doi.org/10.1038/nprot.2011.428

Schafer, D.P., S. Jha, F. Liu, T. Akella, L.D. McCullough, and M.N. Rasband. 2009. Disruption of the axon initial segment cytoskeleton is a new mechanism for neuronal injury. *J. Neurosci.* 29:13242–13254. http://dx.doi.org/10.1523/JNEUROSCI.3376-09.2009

Scott, D.A., U. Das, Y. Tang, and S. Roy. 2011. Mechanistic logic underlying the axonal transport of cytosolic proteins. *Neuron.* 70:441–454. http://dx.doi.org/10.1016/j.neuron.2011.03.022

Sekimoto, S., T. Tashiro, and Y. Komiya. 1991. Two 68-kDa proteins in slow axonal transport belong to the 70-kDa heat shock protein family and the annexin family. *J. Neurochem.* 56:1774–1782. http://dx.doi.org/10.1111/j.1471-4159.1991.tb02080.x

Song, Y., M. Kang, G. Morfini, and S.T. Brady. 2016. Fast axonal transport in isolated axoplasm from the squid giant axon. *Methods Cell Biol.* 131:331–348. http://dx.doi.org/10.1016/bs.mcb.2015.07.004

Tabb, D.L., W.H. McDonald, and J.R. Yates III. 2002. DTASelect and Contrast: Tools for assembling and comparing protein identifications from shotgun proteomics. *J. Proteome Res.* 1:21–26. http://dx.doi.org/10.1021/pr015504q

Takamori, S., M. Holt, K. Stenius, E.A. Lemke, M. Grønborg, D. Riedel, H. Urlaub, S. Schenck, B. Brügger, P. Ringler, et al. 2006. Molecular anatomy of a trafficking organelle. *Cell.* 127:831–846. http://dx.doi.org/10.1016/j.cell.2006.10.030

Tang, Y., U. Das, D.A. Scott, and S. Roy. 2012. The slow axonal transport of alpha-synuclein—mechanistic commonalities amongst diverse cytosolic cargoes. *Cytoskeleton (Hoboken).* 69:506–513. http://dx.doi.org/10.1002/cm.21019

Tang, Y., D. Scott, U. Das, D. Gitler, A. Ganguly, and S. Roy. 2013. Fast vesicle transport is required for the slow axonal transport of synapsin. *J. Neurosci.* 33:15362–15375. http://dx.doi.org/10.1523/JNEUROSCI.1148-13.2013

Terada, S., M. Kinjo, and N. Hirokawa. 2000. Oligomeric tubulin in large transporting complex is transported via kinesin in squid giant axons. *Cell.* 103:141–155. http://dx.doi.org/10.1016/S0092-8674(00)00094-5

Tsai, M.Y., G. Morfini, G. Szebenyi, and S.T. Brady. 2000. Release of kinesin from vesicles by hsc70 and regulation of fast axonal transport. *Mol. Biol. Cell.* 11:2161–2173. http://dx.doi.org/10.1091/mbc.11.6.2161

Twelvetrees, A.E., S. Pernigo, A. Sanger, P. Guedes-Dias, G. Schiavo, R.A. Steiner, M.P. Dodding, and E.L. Holzbaur. 2016. The dynamic localization of cytoplasmic dynein in neurons is driven by kinesin-1. *Neuron.* 90:1000–1015. http://dx.doi.org/10.1016/j.neuron.2016.04.046

Tytell, M., M.M. Black, J.A. Garner, and R.J. Lasek. 1981. Axonal transport: each major rate component reflects the movement of distinct macromolecular complexes. *Science.* 214:179–181. http://dx.doi.org/10.1126/science.6169148

Vale, R.D. 2003. The molecular motor toolbox for intracellular transport. *Cell.* 112:467–480. http://dx.doi.org/10.1016/S0092-8674(03)00111-9

Wang, L., C.L. Ho, D. Sun, R.K. Liem, and A. Brown. 2000. Rapid movement of axonal neurofilaments interrupted by prolonged pauses. *Nat. Cell Biol.* 2:137–141.

Wang, L., U. Das, D.A. Scott, Y. Tang, P.J. McLean, and S. Roy. 2014. α-synuclein multimers cluster synaptic vesicles and attenuate recycling. *Curr. Biol.* 24:2319–2326. http://dx.doi.org/10.1016/j.cub.2014.08.027

Washburn, M.P., D. Wolters, and J.R. Yates III. 2001. Large-scale analysis of the yeast proteome by multidimensional protein identification technology. *Nat. Biotechnol.* 19:242–247. http://dx.doi.org/10.1038/85686

Xu, T., S.K. Park, J.D. Venable, J.A. Wohlschlegel, J.K. Diedrich, D. Cociorva, B. Lu, L. Liao, J. Hewel, X. Han, et al. 2015. ProLuCID: An improved SEQUEST-like algorithm with enhanced sensitivity and specificity. *J. Proteomics.* 129:16–24. http://dx.doi.org/10.1016/j.jprot.2015.07.001

Yuan, A., R.G. Mills, J.R. Bamburg, and J.J. Bray. 1999. Cotransport of glyceraldehyde-3-phosphate dehydrogenase and actin in axons of chicken motoneurons. *Cell. Mol. Neurobiol.* 19:733–744. http://dx.doi.org/10.1023/A:1006953022763

Zhong, G., J. He, R. Zhou, D. Lorenzo, H.P. Babcock, V. Bennett, and X. Zhuang. 2014. Developmental mechanism of the periodic membrane skeleton in axons. *eLife.* 3:e04581. http://dx.doi.org/10.7554/eLife.04581